

RESEARCH ARTICLE

Influence of particle size and shape on the rate of hydrogen produced by Al-doped SrTiO₃ photocatalysts

Mingyi Zhang  | Paul A. Salvador  | Gregory S. Rohrer 

Department of Materials Science and Engineering, Carnegie Mellon University, Pittsburgh, Pennsylvania, USA

Correspondence

Gregory S. Rohrer, Department of Materials Science and Engineering, Carnegie Mellon University, Pittsburgh, PA, USA.

Email: gr20@andrew.cmu.edu

Abstract

Photocatalytic hydrogen production rates have been measured from Al-doped SrTiO₃ with a range of controlled shapes and sizes using a high-throughput parallelized and automated photochemical reactor. It is found that the photocatalytic reactivity is influenced by crystal shape and that crystals with a {110} to {100} surface area ratio between 1.3 and 1.8 yield more H₂ than crystals with other ratios. Crystals with a {110}/{100} surface area ratio of 1.8 generate hydrogen at 550 μmol h⁻¹ g⁻¹ at pH 7, whereas crystals with only {100} facets exposed generate hydrogen at 300 μmol h⁻¹ g⁻¹ under the same condition. It is likely that the surface area ratio provides the appropriate balance between the photoanodic reaction on the {110} surface and the photocathodic reaction on the {100} surface. In the size range of 250–450 nm, larger crystals produce hydrogen at a rate of 400 μmol h⁻¹ g⁻¹ at pH 7, whereas smaller crystals only produce 200 μmol h⁻¹ g⁻¹, suggesting that the larger crystals reduce the rate of electron-hole recombination or back reaction and that the widths of the space charges within the crystal are comparable to the particle radius.

KEYWORDS

doping, hydrogen generation, photocatalysis, strontium titanate

1 | INTRODUCTION

Photocatalytic water splitting is a promising technology to reduce humanity's dependence on fossil fuels by converting solar energy to clean and sustainable H₂ fuel. Since the discovery of photoelectrochemical water oxidation using a TiO₂ photoanode by Fujishima and Honda,¹ thousands of semiconductor materials have been reported to be able to split water.^{2–4} Among them, SrTiO₃ is one of the promising materials with a bandgap of approximately 3.2 eV that can

split water under UV illumination and has been widely studied.^{5,6} Many researchers focus on doping aliovalent metal cations into SrTiO₃ to control the defect structure and improve photocatalytic reactivity.^{7,8} In recent studies, it was found that a flux treatment in SrCl₂—together with Al doping—can significantly increase the reactivity of SrTiO₃ for water splitting.^{9–11} Previous experiments have shown that modifying the band bending in the space charge region either by internal or external electric fields influences the photochemical reactivity.^{12–14} The current

This is an open access article under the terms of the [Creative Commons Attribution-NonCommercial-NoDerivs](https://creativecommons.org/licenses/by-nc-nd/4.0/) License, which permits use and distribution in any medium, provided the original work is properly cited, the use is non-commercial and no modifications or adaptations are made.

© 2022 The Authors. *Journal of the American Ceramic Society* published by Wiley Periodicals LLC on behalf of American Ceramic Society.

study was undertaken to understand how crystal shape and size influence the rate of photocatalytic H₂ yield from Al-doped SrTiO₃.

It is known that particle shapes, because of the facets exposed, influence photocatalytic performance.^{15–17} It is thought that the spatial separation of charge to different exposed facets leads to increased reactivity. For example, Li et al.^{18,19} found the spatial separation of photogenerated electrons and holes among {110} and {010} facets in BiVO₄ contributed to an enhancement of photocatalytic water oxidation reactivity. Previous studies of SrTiO₃ have shown that the {100} surfaces are photocathodic and {110} surfaces are photoanodic,^{20–22} and this is supported by electronic band structure calculations showing that the conduction and valence band edges at the {110} surface are at a higher energy than at {100}.^{20,23} Also, atomic force microscopy (AFM) measurements confirm that {110} surfaces have a more negative surface charge compared with {100} surfaces and are more favorable to photoanodic reactions.²⁴ Besides, SrTiO₃ nanocrystals with both {100} and {110} facets exposed are much more reactive than SrTiO₃ nanocubes (exposing only {100} facets) for photocatalytic water splitting.^{22,25} A more recent paper²⁶ reports that SrTiO₃ particles with {100} and {110} surfaces have reactivities that are inferior to those with only {100} surfaces, but the catalyst particles were significantly smaller than those in the previous work.^{11,22,25} Although previous studies focus on nominally pure SrTiO₃, the effect of shape on the much more reactive Al-doped SrTiO₃ is not yet known. It is found that Al-doped SrTiO₃ treated in SrCl₂ melt showed superior performance for overall water splitting and Takata et al.¹¹ demonstrated a quantum efficiency for overall water splitting up to 96% at 350–360 nm using faceted Al-doped SrTiO₃ particles with different cocatalysts selectively photodeposited on {100} and {110} facets. One of the goals of this paper is to determine the optimal shape for Al-doped SrTiO₃. For example, it has been shown that anatase TiO₂ particles exposing {001} and {101} facets at a ratio of 1.25 are optimal for the photocatalytic reduction of CO₂ to CH₄.²⁷ In this work, we will compare catalyst particles with only photocathodic {100} surfaces to particles that have increasing relative areas of photoanodic {110} surfaces.

Particle sizes are also important to photochemical reactions. In general, smaller particles usually have a higher surface area and more reaction sites at constant mass, and this potentially increases the photochemical reaction rate. However, smaller particles are not always better. If the particle size is less than twice the width of the space charge, band bending will be reduced, lowering the potential to separate electrons and holes.²⁸ Quantum confinement can increase the bandgap of smaller particles,^{29,30} leading to decreased light absorption and reactivity. Finally, the

smallest particles are usually produced at relatively low temperature and may have a higher concentration of structural defects, which typically promote recombination and reduce reactivity. On the other hand, there is clearly an upper limit for particle size. If the particle is too large, charge carriers generated in the flat band region at the center of the crystal are more likely to recombine than to migrate to the surface. The existence of an optimal particle size has been demonstrated for TiO₂,³¹ PbTiO₃,³² and WO₃.³³ One of the goals of this work is to determine if there is an optimal size for Al-doped SrTiO₃ and whether this optimum is a function of particle shape.

The purpose of this work is to understand the influences of crystal shape and size on the rate of H₂ generation by Al-doped SrTiO₃. Catalyst particles with {110}/{100} surface area ratios from 0 to 2.5 have been tested, with particle diameters of ≈250, 350, and 450 nm. All catalysts were treated in an SrCl₂ flux at 1150°C for 10 h containing 1 mol% added Al₂O₃ and afterward loaded with an RhCrO_x cocatalyst. Photocatalytic water splitting experiments have been carried out using the parallel and automated photochemical reactor with particles either in deionized (DI) water whose pH has been adjusted from pH 2 to pH 12 or in 10% aqueous methanol solutions. The rate of H₂ production is found to vary with the crystal shape and size and these variations are consistent with expected changes in subsurface band bending.

2 | METHODS

2.1 | Synthesis of catalysts

SrTiO₃ crystals were prepared hydrothermally following a procedure reported by Dong et al.³⁴ Four types of crystals, denoted as A, B, C, and D, were prepared in an identical fashion with the exception of the surfactant used. In all cases, 0.2 ml of pure TiCl₄ (Sigma-Aldrich, 99%) was dropped into a solution in an ice bath containing 25 ml of DI water and the surfactant. These types and amounts of surfactants were used to generate large crystals with an average diameter of 450 nm: A—2 g of ethanol (PHARMCO, 200 Proof), B—1 g of 1,2-propanediol (Sigma-Aldrich, 99.5%), C—1 g of ethylene glycol (Alfa Aesar, 99+%), and D—0.1 g of pentaerythritol (Sigma-Aldrich, 99%). After magnetic stirring for 5 min, 10 ml of 0.265-M SrCl₂ solution containing 0.42-g SrCl₂ (Sigma-Aldrich, 99.99%) and 30 ml of 3-M LiOH solution containing 2.16-g LiOH (Sigma-Aldrich, 98%) was added. After stirring for another 30 min, the resulting solution was transferred to a 100-ml Teflon-lined hydrothermal autoclave (Techinstro). The autoclave was then heated at 180°C for 36 h in a furnace. After heat treatment, the solution was removed

TABLE 1 Summary of synthesis route and conditions for all samples

Catalysts	Shape	Type of surfactant	Amount of surfactant (g)	Average size (nm)
A-L	(100) facet only	Ethanol	2	450
B-L	(110)/(100) = 1.3	1,2-Propanediol	1	450
C-L	(110)/(100) = 1.8	Ethylene glycol	1	450
D-L	(110)/(100) = 2.5	Pentaerythritol	0.1	450
A-M	(100) facet only	Ethanol	10	350
A-S	(100) facet only	Ethanol	20	250
B-M	(110)/(100) = 1.3	1,2-Propanediol	6	350
B-S	(110)/(100) = 1.3	1,2-Propanediol	12	250

and the resulting precipitate was centrifugated, washed alternatively with water and ethanol four times each at 4000 rpm for 12 min. Finally, the resulting precipitate was dried in an oven at 80°C overnight. Additionally, SrTiO₃ crystals of type A (type B) were also prepared in two smaller sizes, with average diameters of 350 and 250 nm, referred to as medium and small, following the same procedure but increasing the amount of surfactant to 10 g (6 g) for medium and 20 g (12 g) for small. All samples' abbreviations and corresponding synthesis conditions are summarized in Table 1.

Note that during the hydrothermal synthesis, an excess of SrCl₂, greater than the stoichiometric ratio for SrTiO₃, was employed. In initial experiments where the stoichiometric ratio was used, the product was a mixture of anatase, rutile, and SrTiO₃. These small TiO₂ particles adhere to the larger SrTiO₃ crystals and blocked the illumination. By adding an excess amount of SrCl₂ in the hydrothermal synthesis, the formation of TiO₂ was inhibited, and clean SrTiO₃ crystals with reproducible morphologies were obtained. It is also noted that the crystals synthesized in our lab have a larger size compared to what is reported by Dong et al.,³⁴ even though the same amounts of surfactants are added.

SrTiO₃ nanocrystals of types A, B, C, and D were doped with Al in a SrCl₂ flux, as described by Domen and coworkers.^{10,11} The hydrothermally grown SrTiO₃, Al₂O₃ nanopowders (Sigma-Aldrich, <50-nm particle size), and SrCl₂ (Alfa Aesar, 99.5%) were mixed at a molar ratio of 1:0.01:10 with mortar and pestle. The mixture was then heated at 1150°C for 10 h in an alumina crucible, a temperature at which the SrCl₂ liquifies. To remove the SrCl₂ thoroughly after the process, the resulting mixture was centrifugated first with DI water and then with ethanol, four times each at 4000 rpm for 12 min. The resulting Al-doped SrTiO₃ powders were then dried in an oven at 80°C overnight.

RhCrO_x cocatalysts were loaded (0.1-wt% Rh and 0.1-wt% Cr) on all crystals with an impregnation method

described elsewhere.³⁵ An amount of 50-mg as-prepared Al-doped SrTiO₃ crystals was dispersed into 0.5 ml of DI water containing appropriate amounts of Na₃RhCl₆ (Sigma-Aldrich) and Cr(NO₃)₃·6H₂O (Sigma-Aldrich, 99%) to yield 0.1-wt% Rh and Cr. Note that, in some experiments, this amount was adjusted to study the effect of the amount of cocatalysts loaded on the reactivity. The suspension was evaporated in a water bath under constant manually stirring. The resulting powders were collected and heated at 350°C for 1 h. A schematic illustration of the catalyst synthesis route is presented in Figure 1.

P25 TiO₂ was used as a reference catalyst and included in all panels, so that results could be compared from panel to panel. P25 powders were loaded with 1-wt% Pt by the impregnation method.^{36,37} P25 powders (Degussa) were immersed in an H₂PtCl₆ solution (Sigma-Aldrich) for 2 h with magnetic stirring. Then, the powders were reduced using a fivefold excess of NaOH (Fisher Scientific) and NaBH₄ (Acros) for 2 h with stirring. The powders were then collected and rinsed in DI water by centrifugation and dried overnight.

2.2 | Characterization

The phase of each sample was determined with powder X-ray diffraction (XRD) using an X'Pert Pro MPD X-ray diffractometer (PANalytical, Philips, The Netherlands) equipped with a high-intensity (45 kV, 40 mA) Cu K α radiation source ($K\alpha 1 = 1.5406 \text{ \AA}$, $K\alpha 2 = 1.5444 \text{ \AA}$). A scan rate of 5°-min⁻¹ was applied in the range of 20°–90° at a step size of 0.02°. Scanning electron microscopy (SEM) images were obtained to determine the morphologies of all samples using FEI Quanta 600 with a 20-kV beam with a spot size of 3. An Oxford full analytical XMAX 80-mm SDD EDX detector was equipped on the SEM for chemical composition analysis. N₂ adsorption-desorption measurements (NOVA 2200E, Quantachrome, FL), used to determine the specific surface areas of powders through

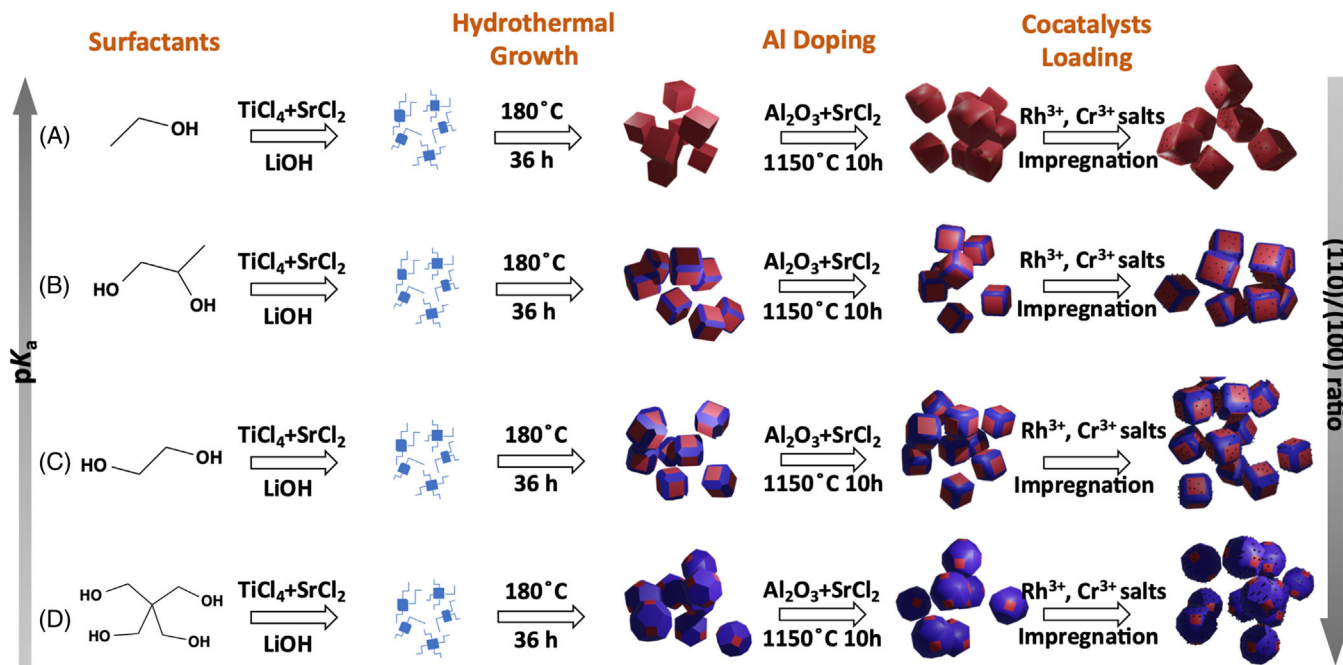


FIGURE 1 Schematic diagram illustrating the route of formation of Al-doped SrTiO_3 catalysts in the presence of different surfactants. A, B, C, and D are the designations for the different particle shapes

a Brunauer–Emmett–Teller (BET) approach, were performed at 77 K using a multipoint method. The sample was degassed at 110 °C for 24 h prior to measurement. UV–vis diffuse reflectance spectra were recorded on an OL 770 Multi-Channel Spectroradiometer (Optronic Laboratories).

2.3 | Photocatalytic water splitting experiment

The photocatalytic reactivity for hydrogen evolution was measured with a high-throughput parallelized and automated photochemical reactor (PAPCR), illustrated schematically in Figure 2.³⁸ Two 100-W UV LED chips (Chanzone, 380 nm) at the bottom of the reactor were fixed on an aluminum plate to provide constant illumination for the reaction. The LEDs were cooled by a fan and circulating chilled water. At the mid part of the reactor, 108 1-ml borosilicate glass shell vials sit on an aluminum plate with small holes drilled at the bottom, through which illumination from the LEDs can transmit into the vials. The vials were covered with a layer of hydrogen-sensitive film (DetecTape, Midsun Specialty Products) whose color changes from light to dark with an increase in the local hydrogen concentration. A typical image of the panel before and after reactions is shown in Figure S1a,b. A fluorinated ethylene propylene (FEP) film was placed on top of the hydrogen-sensitive film to create a

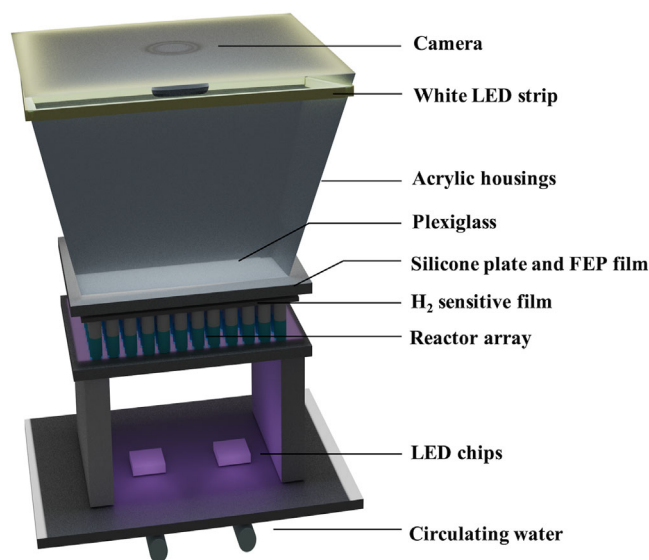


FIGURE 2 Schematic illustration of the PAPCR. PAPCR, parallelized and automated photochemical reactor

gas-impermeable environment. Next, a flexible silicone layer and a rigid plexiglass plate were placed on the top of the FEP film to seal and cover the whole reactor array. At the top of the reactor, a Pi camera (Raspberry Pi Camera Board V2, 8 Megapixels) was fixed. In every 6 min, the LEDs are switched off and the camera takes a picture of the hydrogen-sensitive film. After the picture was taken, the LEDs were switched on for another 6-min cycle. Two

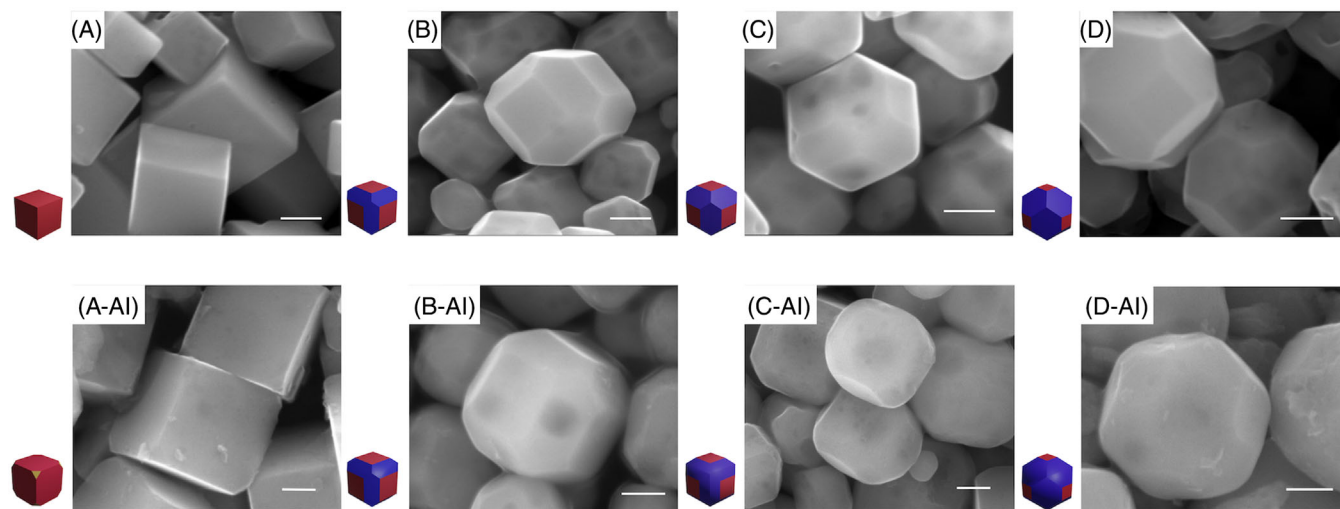


FIGURE 3 SEM images, as well as schematic diagrams, for different types (columns) of SrTiO₃ nanocrystals that were undoped (top row) or were treated in melts with 1% Al added (bottom row). Scale bar is 200 nm. SEM, scanning electron microscopy. The different particle shapes are denoted A, B, C, and D. The suffix-Al is added to that have been doped with Al

rows of white LED strips (JUNWEN, 16 W) were used to illuminate the hydrogen-sensitive tape from above while the image was captured. For each image, the RGB values were extracted for an area of 54 pixels in the center of each vial to determine the darkness of the film. These values were then subtracted from the darkness value from the first image. The response of the hydrogen-sensitive film was calibrated in the range of 4%–31% of H₂, shown in Figure S1c and Table S1, by adding known amounts of hydrogen to the vials and recording the response. Based on the calibrated relationship between local hydrogen concentration and the appearance of the film, it is possible to calculate the amount of H₂ production every 6 min and, from such data shown in Figure S1d, the reaction rate.

By varying the amount of Al-doped SrTiO₃ added to each vial, we found that the absolute rate ($\mu\text{mol h}^{-1}$) of H₂ evolution reached the maximum at 10 mg (see Figure S2). Therefore, in all further experiments, 10 mg of Al-doped SrTiO₃ was added to each shell vial with 0.6 ml of DI water whose pH was adjusted from pH 2 to pH 12 by adding acetic acid (Fisher Chemical) or NaOH (Fisher Scientific). The reactor was illuminated for 18 h, during which a total of 180 images were taken, with each image quantifying the hydrogen concentration within each vial. We verified that the acid anion group did not significantly influence reactivity by comparing reaction rates of the same sample in DI water whose pH was adjusted using acetic acid, nitric acid, or hydrochloric acid. The results are shown in Figure S3 and confirm that the type of acid does not influence reactivity. To determine the effect of adding a hole scavenger, a parallel set of experiments was conducted with solutions containing 10% methanol and 5 mg of catalyst. Each experiment included three vials with 3.2 mg of the P25 reference

catalyst in 6 ml of a 1% methanol solution. The standard deviation was calculated from the H₂ production rates of the three reference catalysts.

3 | RESULTS

SEM images of shape-controlled SrTiO₃ particles before and after Al doping in molten SrCl₂ are shown in Figure 3. Focusing on the undoped crystals in the top row, crystals of type A (left top) are cubes, exposing only six {100} facets. Crystals of types B, C, and D, shown from left to right, are edge-truncated cubes, exposing both {100} and {110} facets, where the ratios of the {110} areas to the {100} areas are 1.3, 1.8, and 2.5 for B, C, and D, respectively. The different crystal shapes result from the different surfactants added. A surfactant with relatively lower pK_a value will have a stronger interaction with the (110) facet, adjusting the surface energy and reducing the growth rate, leading to a greater fraction of exposed (110) facets, according to the mechanism explained by Dong et al.³⁴ Schematic drawings of the possible (100) and (110) surface terminations are shown in Figure S4 and a schematic illustration of how to calculate the area ratio of the two facets is shown in Figure S5. After Al-doping (the second row in Figure 3), the sharp edges between the facets appear less defined and, for the case of some shape A particles, small {111} facets are introduced at the corners. With the exception of these two small changes, the SrCl₂ flux treatment does not alter the shapes of the crystals. All crystals have similar sizes with an average diameter of 450 nm, and the Al-doping treatment did not have an obvious influence on the particle size. The BET surface areas of the particles are all

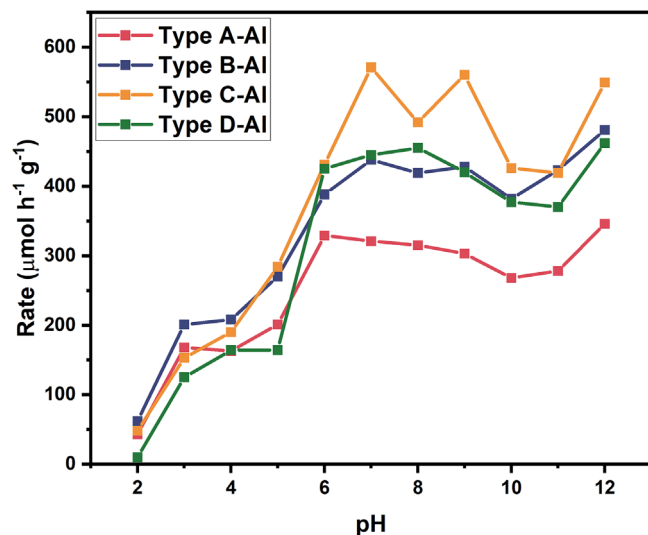


FIGURE 4 Mass-specific rate of hydrogen generation from suspensions with four types of Al-doped SrTiO₃ powders in DI water whose pH is in the range of 2–12. The standard deviation is 11%. DI, deionized

between 3.2 and 4.3 m² g⁻¹ (Table S2), similar to the ideal computed surface area for a 450-nm diameter SrTiO₃ cube (2.9 m² g⁻¹). XRD patterns of the Al-doped SrTiO₃ samples are given in Figure S6 and all strong peaks are attributed to SrTiO₃. The reference lattice parameter of SrTiO₃ (ICDD: 01-073-0661) is 3.9050 Å, and the lattice parameters of our samples (refined with HighScore) were very close to this value. For samples A-Al, B-Al, C-Al, and D-Al, the lattice parameters were 3.9051(1), 3.9047(2), 3.9044(2), and 3.9045(2) Å, respectively. Some low-intensity peaks found in the patterns can be attributed to rutile and anatase TiO₂ formed during the hydrothermal synthesis and some unreacted Al₂O₃. Because these impurity phases are present in small amounts, and all samples have similar amounts of these phases, we do not expect that this will impact the experimental results significantly. To confirm the stoichiometry of the product phase, EDS analyses were carried out on all samples, as shown in Figure S7. It is found that, for all shapes, the atomic ratios of Sr, Ti, and O are roughly 1:1:3, and the Al concentration varies from 0.81% to 0.9%.

The mass-specific rates (μmol h⁻¹ g⁻¹) of H₂ evolution from the Al-doped SrTiO₃ crystals shown in Figure 3 were measured under UV illumination at 380 nm using the PAPCR, and the results are shown in Figure 4. The standard deviation is about 12% (11%) for shapes A and B (C and D). Because all the catalysts have similar surface areas, the surface area-specific rates (μmol h⁻¹ m⁻²) are almost the same (see Figure S8). As shown in Figure 5, the bandgap energies of the crystals are also essentially the same (3.28, 3.27, 3.26, and 3.27 eV for types A, B, C, and D, respectively), so differences in absorption are not expected to

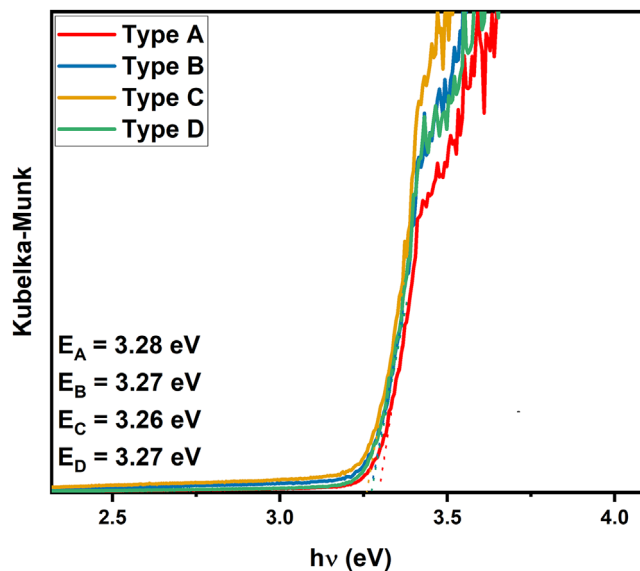


FIGURE 5 UV-vis diffuse reflectance spectra of four types of Al-doped SrTiO₃

influence the reactivity. The corresponding reflectance and absorbance spectra are given in Figure S9. Several trends are apparent from Figure 4. First, crystals of types of B, C, and D produce H₂ at a greater rate than A. This was also true when the reaction was carried out in 10% methanol solutions (see Figure S10). Second, for all types of crystals, the reactivity first increases with pH to a maximum at around pH 7 then decreases at pH 10 and pH 11. At pH 12, there is usually an increase in reactivity. The initial increase in reactivity with pH is consistent with observations reported for undoped SrTiO₃ single crystals.³⁹ This is likely due to an increase in the absorption of negative charge with increasing pH that bends the bands further upward and promotes the conduction of holes to the surface. Although this increase of the upward band bending will increase the energy barrier for electrons to migrate to the surface, the overall photocatalytic reaction rate depends on the slower of the two half reactions. Therefore, the reaction rate will be first limited by the photoanodic reaction at low pH and then the photocathodic reaction at a higher pH. The maximum reactivity should appear at an intermediate pH where neither the photocathodic nor the photoanodic reaction limits the overall reaction rate. Crystals without deliberate Al additions and not treated in the SrCl₂ flux did not generate enough H₂ to exceed the lower calibrated limit of the PAPCR either in pure water or methanol solutions (and are not shown here). We have also prepared and tested crystals with higher concentrations of added Al and found that, for all shapes, crystals with 1% Al added yielded the most hydrogen, as shown in Figure S11.

To investigate the influence of particle size on the photocatalytic reactivity, Al-doped SrTiO₃ of shapes A and

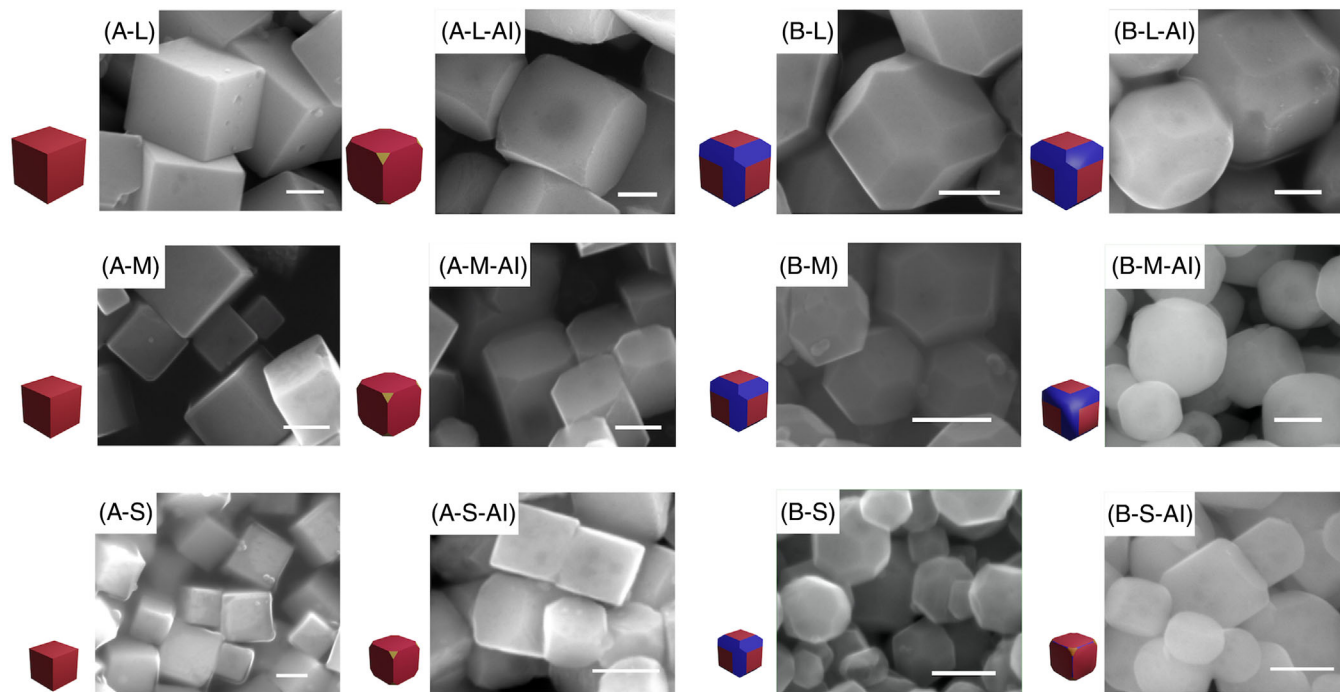


FIGURE 6 SEM images as well as schematic diagrams for type A and B SrTiO_3 crystals with large, medium, and small size. Scale bar = 200 nm. SEM, scanning electron microscopy

B were prepared with different sizes, by increasing the amount of surfactant in the hydrothermal synthesis. SEM images of the 12 kinds of crystals are shown in Figure 6 and the corresponding particle size distributions are given in Figure S12. Large (≈ 450 nm), medium (≈ 350 nm), and small crystals (≈ 250 nm) of types A and B are given in rows in Figure 6, respectively, from top to bottom and are labeled A-L (B-L), A-M (B-M), and A-S (B-S), respectively, with an -Al appended to the name when samples were aluminum doped. The L, M, and S particles had size distributions of ± 50 nm. Note that all crystals in Figure 3 are large. Consistent with the prior experiments, Al doping rounded the edges of type B crystals and introduced small $\{111\}$ facets on type A crystals. The Al-doped B-S type crystals changed to a near cube shape, as for type A.

The mass-specific hydrogen evolution rates of the six types of Al-doped samples are shown in Figure 7. We found that, for both crystal shapes, in the range of 250–450 nm, the photocatalytic reactivity increased with sizes and the largest crystals were the most reactive. The surface area-specific hydrogen generation rates for these materials are shown in Figure S13 and have nearly the same trend with size. The trends with solution pH were consistent with the results described in Figure 4. Note that, although the A-L and B-L crystals in this experiment were from a different batch than the crystals in Figure 4, their reactivities were similar, illustrating that the results are reproducible. For type B crystals, the crystal shape changed with Al doping,

so the results are influenced by both the particle shape and size. The crystals of type A provide the most convincing evidence of the size effect because their shapes are nearly the same under all conditions. Using solutions with 10% methanol did not change the trend in the relative amounts of hydrogen (see Figure S14).

Although we have found that the hydrogen evolution rate decreased with decreasing particle sizes for both type A and type B Al-doped SrTiO_3 s, we loaded the same amount of RhCrO_x cocatalyst on these crystals. Considering the fact that crystals with the medium size and small size have larger surface areas, as shown in Table S2, one might argue that these smaller crystals should have more cocatalyst loaded to maintain a constant amount of cocatalyst per area. Therefore, using shape type B crystals, we changed the cocatalyst loading on the three sizes to maintain a constant coverage per surface area. Based on BET data, the surface areas for B-L, B-M, B-S nanocrystals were 3.2, 6.7, and 10 $\text{m}^2 \text{g}^{-1}$, which was roughly in the proportion of 1:2:3. Therefore, we loaded 0.1, 0.2, and 0.3 wt% RhCrO_x (metal ratio) on B-L, B-M, and B-S nanocrystals, respectively and measured their H_2 generation rates. As shown in Figure S15, B-L-type crystals still had the highest H_2 generation rate. It is found that increasing the amount of cocatalyst did not increase, but rather decreased, the photocatalytic reactivity for B-M and B-S crystals. As a result, we believe that the relatively lower reactivity of the smaller crystals was not because they had a smaller cocatalyst

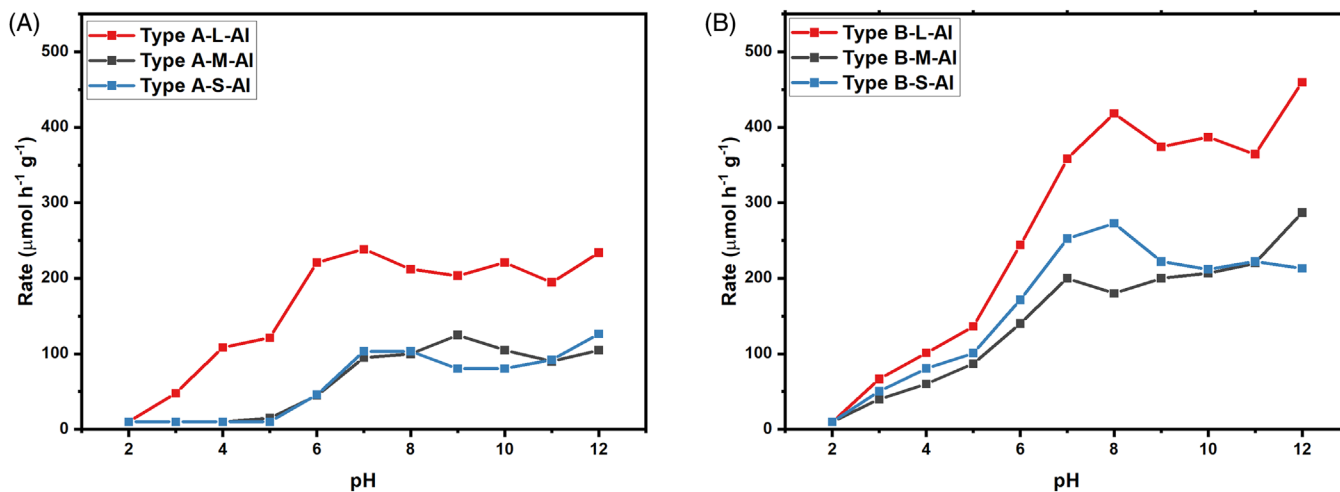


FIGURE 7 Mass-specific rates of hydrogen production ($\mu\text{mol h}^{-1} \text{g}^{-1}$) from suspensions with crystal types A-L, A-M, and A-S in DI water whose pH is in the range of 2–12 are shown in (A). The standard deviation is 12%. Mass-specific rates of hydrogen production ($\mu\text{mol h}^{-1} \text{g}^{-1}$) from suspensions with crystal types B-L, B-M, and B-S in DI water are shown in (B), whose pH is in the range of 2–12. The standard deviation is 10%. DI, deionized

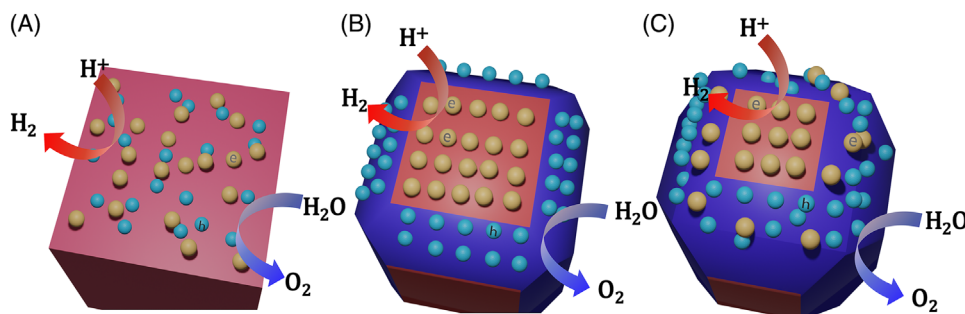


FIGURE 8 Schematic illustration of the spatial distribution of photogenerated electrons and holes on (A) {100} facets dominated, (B) an optimal ratio of {100} to {110} facets, (C) {110} facet-dominated conditions. Red surface and blue surface represent {100} and {110} facets. Yellow balls and blue balls represent electrons and holes

coverage. On the contrary, loading more cocatalyst further decreased the reactivity. It would be interesting to test even larger crystals, because we expect that at some point, the reactivity should decrease with the increased size, but we have not been able to synthesize larger crystals with controlled shapes.

4 | DISCUSSION

4.1 | Effect of particle shape

The results described here show that the rate of hydrogen production from Al-doped SrTiO_3 is influenced by crystal shape. The results show that type C crystals had the highest mass-specific rate ($\mu\text{mol h}^{-1} \text{g}^{-1}$) with the {110} to {100} surface area ratio equal to 1.8. Increases or decreases in this ratio lower the reactivity. This can be

understood by the schematic diagrams in Figure 8 and the fact that the {110} surface is photoanodic in comparison to {100}, which is relatively photocathodic.^{21,22} The finding that electrons (holes) migrate to {100} ({110}) surfaces of these particles is validated by the data in Figure S16, which shows that Ag^+ (Mn^{2+}) is reduced (oxidized) on the {100} ({110}) surfaces. For the shape with the ideal reactivity, equal numbers of electrons and holes migrate to the {100} and {110} surfaces, respectively, where they can contribute to the reaction. However, if there are no {110} facets (see Figure 8A), then holes must also migrate to the {100} surfaces, where they are likely to recombine with electrons, lowering reactivity; this is the case for type A crystals. The opposite case, where there is insufficient photocathodic {100} area to support the reduction reaction, is shown in Figure 8C and represents type D crystals. In this case, the reduction in the rate of the cathodic reaction and the likely increased rate of recombination will limit the rate of the

overall reaction. It is noted that, after normalizing by surface area, type C crystals still have the best surface area-specific rates ($\mu\text{ mol h}^{-1}\text{ m}^{-2}$) at pH 7, but type B crystals show a higher reactivity at pH 12. This implies that if we could synthesize particles with a $\{110\}$ to $\{100\}$ surface area ratio between 1.3 and 1.8, the photocatalytic reactivity might be further optimized.

4.2 | Effect of particle size

The measurements of the rate of hydrogen evolution from crystals of different sizes indicated that the reactivity increases with crystal size, from 250 to 450 nm. This is counterintuitive, considering that the mass-specific surface area decreases as the particle size increases. Changes in the reactivity with size are sometimes ascribed to the quantum size effect.^{40,41} However, quantum size effects are expected only in crystals much smaller than those considered here. We note that Hsieh et al.²⁵ reported that the bandgap of 290-nm SrTiO_3 was 31 meV smaller than 160-nm SrTiO_3 , but this difference would not increase the absorption enough to account for the increased reactivity.

There are two plausible explanations for the increase in reactivity of the larger crystals. One possible explanation for the observed size effect is that the reaction is limited by the back reaction of neutral H and hydroxyl radicals on or near the surface. As the particle size decreases, these species are produced in closer proximity, so they do not have to diffuse as far to recombine, and this might limit the reaction rate. However, according to Turchi and Ollis,⁴² the diffusion of hydroxyl radicals is fast compared to the rate of reaction with the semiconductor surface and with the other species in solution, so the effect of increasing the particle size on the rate of the back reaction is not expected to be significant.

Another explanation is that the space charge layer beneath the surface is large compared to the particle size. One of the parameters influencing the depth of the space charge in SrTiO_3 is the carrier concentration. Past studies agree that SrTiO_3 with no intentionally added impurities is an acceptor doped n-type semiconductor.^{43,44} The n-type electronic properties result from electrons ionized from oxygen vacancies ($V_{\text{O}}^{\bullet\bullet}$) and measurements indicate that the concentration of oxygen vacancies is much greater than the concentration of acceptor impurities. Therefore, the electroneutrality condition is $2[V_{\text{O}}^{\bullet\bullet}] \approx n$ where n is the concentration of ionized electrons and $n \approx 10^{19}\text{ cm}^{-3}$.⁴⁴ However, the added Al acts as an acceptor dopant (Al_{Ti}) that can compensate for the oxygen vacancies and reduce the electron concentration. Calculations based on data in the literature,⁴⁵ described in the Supplemental Information, show that when SrTiO_3 is fully compensated by a

small amount of dissolved Al, the carrier concentration is reduced to as low as $n \approx 10^{16}\text{ cm}^{-3}$ at the temperature of the SrCl_2 flux. At room temperature, where the catalyst is used, the carrier concentration of ideally compensated SrTiO_3 falls to $n \approx 10^{12}\text{ cm}^{-3}$.⁴⁶ This reduction in the carrier concentration would expand the width of the space charge layer (the Debye length) from $\approx 3\text{ nm}$ (in the undoped condition where $n = 10^{19}\text{ cm}^{-3}$) to $\approx 9 \times 10^3\text{ nm}$ (at the point of compensation where $n = 10^{12}\text{ cm}^{-3}$). Not knowing the Al concentration in the samples, we cannot estimate the degree of compensation. However, it is clear that added Al will decrease the carrier concentration and increase the Debye length. Note that a similar mechanism has been proposed to explain the reactivity enhancement that results from Mg doping of SrTiO_3 .⁴⁷ At the wavelength of light used here, the absorption coefficient is on the order of 100 cm^{-1} ,⁴⁸ which implies an absorption depth of 10^4 nm . Because of the large absorption depth, increases in the space charge region result in an increase in the number of photogenerated carriers that can be separated by the field.

As discussed before, the Debye length might be on the order of 10^3 nm . In this case, for particles smaller than this length, the space charges overlap in the center of the crystal. This reduces the difference between the surface and bulk electric potentials and leads to reduced charge separation.²⁸ In the larger crystals, the space charge is more fully developed and there is a larger potential to separate charge. This idea is supported by simulations of the reactivity of BaTiO_3 showing that the difference in electric potential (under illumination) at the surface between positive and negative domains is only 0.17 V for a small 10-nm domain, whereas this difference of potential is 0.60 V for a large 250-nm domain.⁴⁹ The increased space charge depth, together with relatively large absorption depth discussed earlier, should result in increased reactivity. In other words, the larger space charge regions in the larger crystals are more likely to be the cause of their increased reactivity than the suppression of the back reaction by the physical separation of the cathodic and anodic sites.

5 | CONCLUSION

The influence of particle shape and size on the photocatalytic generation of hydrogen by Al-doped SrTiO_3 has been measured. The most suitable shape was determined to be an edge-truncated cube with a $\{110\}$ to $\{100\}$ surface area ratio between 1.3 and 1.8. With this geometry, electrons (holes) move to $\{100\}$ ($\{110\}$) facets and promote the photoreduction (photooxidation) half reaction, a situation that likely reduces the rate of recombination or back reaction. Crystals with diameters around 450 nm are more reactive

than smaller ones, consistent with the presence of wide space charge regions that result from the Al acceptors that reduce the n-type carrier concentration.


ACKNOWLEDGMENTS

This work was supported by the National Science Foundation under Grant Number: DMR 2016267, and the authors acknowledge the use of the Materials Characterization Facility at Carnegie Mellon University supported by Grant Number: MCF-677785. The authors acknowledge E. Lopato, J. Kowalewski, and S. Bernhard for assistance with building and calibrating PAPCR and the assistance from K. Jiang and L. Porter with the optical measurements.

ORCID

Mingyi Zhang  <https://orcid.org/0000-0002-9996-6774>

Paul A. Salvador  <https://orcid.org/0000-0001-7106-0017>

Gregory S. Rohrer  <https://orcid.org/0000-0002-9671-3034>

REFERENCES

- Fujishima A, Honda K. Electrochemical photolysis of water at a semiconductor electrode. *Nature*. 1972;238(5358):37–38.
- Osterloh FE. Inorganic materials as catalysts for photochemical splitting of water. *Chem Mater*. 2008;20(1):35–54.
- Hisatomi T, Domen K. Reaction systems for solar hydrogen production via water splitting with particulate semiconductor photocatalysts. *Nat Catal*. 2019;2(5):387–99.
- Wang Q, Domen K. Particulate photocatalysts for light-driven water splitting: mechanisms, challenges, and design strategies. *Chem Rev*. 2020 Jan 22;120(2):919–85.
- Wrighton MS, Ellis AB, Wolczanski PT, Morse DL, Abrahamson HB, Ginley DS. Strontium titanate photoelectrodes. Efficient photoassisted electrolysis of water at zero applied potential. *J Am Chem Soc*. 1976 May 1;98(10):2774–9.
- Kumar A, Santangelo PG, Lewis NS. Electrolysis of water at SrTiO₃ photoelectrodes: distinguishing between the statistical and stochastic formalisms for electron-transfer processes in fuel-forming photoelectrochemical systems. *J Phys Chem*. 1992;96(2):834–42.
- Takata T, Domen K. Defect engineering of photocatalysts by doping of aliovalent metal cations for efficient water splitting. *J Phys Chem C*. 2009 Nov 12;113(45):19386–8.
- Jiang J, Kato K, Fujimori H, Yamakata A, Sakata Y. Investigation on the highly active SrTiO₃ photocatalyst toward overall H₂O splitting by doping Na ion. *J Catal*. 2020;390:81–9.
- Ham Y, Hisatomi T, Goto Y, Moriya Y, Sakata Y, Yamakata A, et al. Flux-mediated doping of SrTiO₃ photocatalysts for efficient overall water splitting. *J Mater Chem A*. 2016;4(8):3027–33.
- Goto Y, Hisatomi T, Wang Q, Higashi T, Ishikiriya K, Maeda T, et al. A particulate photocatalyst water-splitting panel for large-scale solar hydrogen generation. *Joule*. 2018;2(3):509–20.
- Takata T, Jiang J, Sakata Y, Nakabayashi M, Shibata N, Nandal V, et al. Photocatalytic water splitting with a quantum efficiency of almost unity. *Nature*. 2020;581(7809):411–4.
- Li L, Salvador PA, Rohrer GS. Photocatalysts with internal electric fields. *Nanoscale*. 2014;6(1):24–42.
- Chen F, Huang H, Guo L, Zhang Y, Ma T. The role of polarization in photocatalysis. *Angew Chem Int Ed*. 2019;58(30):10061–73.
- Marschall R. Semiconductor composites: strategies for enhancing charge carrier separation to improve photocatalytic activity. *Adv Funct Mater*. 2014 May;24(17):2421–40.
- Liu G, Yu JC, Lu GQ, Cheng H-M. Crystal facet engineering of semiconductor photocatalysts: motivations, advances and unique properties. *Chem Commun*. 2011;47(24):6763–83.
- Huang MH. Facet-dependent optical properties of semiconductor nanocrystals. *Small*. 2019;15(7):1804726.
- Bai S, Wang L, Li Z, Xiong Y. Facet-engineered surface and interface design of photocatalytic materials. *Adv Sci*. 2017;4(1):1600216.
- Li R, Zhang F, Wang D, Yang J, Li M, Zhu J, et al. Spatial separation of photogenerated electrons and holes among {010} and {110} crystal facets of BiVO₄. *Nat Commun*. 2013;4(1):1432.
- Li R, Han H, Zhang F, Wang D, Li C. Highly efficient photocatalysts constructed by rational assembly of dual-cocatalysts separately on different facets of BiVO₄. *Energy Environ Sci*. 2014;7(4):1369–76.
- Giocondi JL, Salvador PA, Rohrer GS. The origin of photochemical anisotropy in SrTiO₃. *Top Catal*. 2007 Jul;44(4):529–33.
- Pisat AS, Salvador PA, Rohrer GS. The facet structure and photochemical reactivity of arbitrarily oriented strontium titanate surfaces. *Adv Mater Interfaces*. 2019;6(16):1900731.
- Mu L, Zhao Y, Li A, Wang S, Wang Z, Yang J, et al. Enhancing charge separation on high symmetry SrTiO₃ exposed with anisotropic facets for photocatalytic water splitting. *Energy Environ Sci*. 2016;9(7):2463–9.
- Mattheiss LF. Energy bands for KNiF₃, SrTiO₃, KMoO₃, and KTaO₃. *Phys Rev B*. 1972 Dec;6(12):4718–40.
- Su S, Siretanu I, vanden Ende D, Mei B, Mul G, Mugele F. Facet-dependent surface charge and hydration of semiconducting nanoparticles at variable pH. *Adv Mater*. 2021;33:2106229.
- Hsieh P-L, Naresh G, Huang Y-S, Tsao C-W, Hsu Y-J, Chen L-J, et al. Shape-tunable SrTiO₃ crystals revealing facet-dependent optical and photocatalytic properties. *J Phys Chem C*. 2019;123(22):13664–71.
- Vijay A, Vaidya S. Tuning the morphology and exposed facets of SrTiO₃ nanostructures for photocatalytic dye degradation and hydrogen evolution. *ACS Appl Nano Mater*. 2021 Mar 25;4:3406–15.
- Yu J, Low J, Xiao W, Zhou P, Jaroniec M. Enhanced photocatalytic CO₂-reduction activity of anatase TiO₂ by coexposed {001} and {101} facets. *J Am Chem Soc*. 2014 Jun 25;136(25):8839–42.
- Albery WJ, Bartlett PN. The transport and kinetics of photogenerated carriers in colloidal semiconductor electrode particles. *J Electrochem Soc*. 1984 Feb;131(2):315–25.
- Banin U, Cao Y, Katz D, Millo O. Identification of atomic-like electronic states in indium arsenide nanocrystal quantum dots. *Nature*. 1999;400(6744):542–4.
- Peng X, Manna L, Yang W, Wickham J, Scher E, Kadavanich A, et al. Shape control of CdSe nanocrystals. *Nature*. 2000;404(6773):59–61.

31. Zhang Z, Wang C-C, Zakaria R, Ying JY. Role of particle size in nanocrystalline TiO₂-based photocatalysts. *J Phys Chem B*. 1998 Dec 1;102(52):10871–8.
32. Arney D, Watkins T, Maggard PA. Effects of particle surface areas and microstructures on photocatalytic H₂ and O₂ production over PbTiO₃. *J Am Ceram Soc*. 2011 May 1;94(5):1483–9.
33. Amano F, Ishinaga E, Yamakata A. Effect of particle size on the photocatalytic activity of WO₃ particles for water oxidation. *J Phys Chem C*. 2013 Nov 7;117(44):22584–90.
34. Dong L, Shi H, Cheng K, Wang Q, Weng W, Han W. Shape-controlled growth of SrTiO₃ polyhedral submicro/nanocrystals. *Nano Res*. 2014 Sep;7(9):1311–8.
35. Maeda K, Teramura K, Masuda H, Takata T, Saito N, Inoue Y, et al. Efficient overall water splitting under visible-light irradiation on (Ga_{1-x}Zn_x)(N_{1-x}O_x) dispersed with Rh–Cr mixed-oxide nanoparticles: effect of reaction conditions on photocatalytic activity. *J Phys Chem B*. 2006;110(26):13107–12.
36. He Z, Xie L, Tu J, Song S, Liu W, Liu Z, et al. Visible light-induced degradation of phenol over iodine-doped titanium dioxide modified with platinum: role of platinum and the reaction mechanism. *J Phys Chem C*. 2010 Jan 14;114(1):526–32.
37. Li L, Liu X, Zhang Y, Salvador PA, Rohrer GS. Heterostructured (Ba,Sr)TiO₃/TiO₂ core/shell photocatalysts: influence of processing and structure on hydrogen production. *Int J Hydrogen Energy*. 2013;38(17):6948–59.
38. Lopato EM, Eikey EA, Simon ZC, Back S, Tran K, Lewis J, et al. Parallelized screening of characterized and DFT-modeled bimetallic colloidal cocatalysts for photocatalytic hydrogen evolution. *ACS Catal*. 2020 Apr 3;10(7):4244–52.
39. Zhang M, Salvador PA, Rohrer GS. Influence of pH and surface orientation on the photochemical reactivity of SrTiO₃. *ACS Appl Mater Interfaces*. 2020 Apr 24;12:23617–26
40. Norris DJ, Bawendi MG. Measurement and assignment of the size-dependent optical spectrum in CdSe quantum dots. *Phys Rev B*. 1996 Jun;53(24):16338–46.
41. Mora-Seró I, Giménez S, Moehl T, Fabregat-Santiago F, Lana-Villareal T, Gómez R, et al. Factors determining the photovoltaic performance of a CdSe quantum dot sensitized solar cell: the role of the linker molecule and of the counter electrode. *Nanotechnology*. 2008 Sep;19(42):424007.
42. Turchi CS, Ollis DF. Photocatalytic degradation of organic water contaminants: mechanisms involving hydroxyl radical attack. *J Catal*. 1990;122(1):178–92.
43. Shi T, Chen Y, Guo X. Defect chemistry of alkaline earth metal (Sr/Ba) titanates. *Prog Mater Sci*. 2016;80:77–132.
44. Chan N-H, Sharma RK, Smyth DM. Nonstoichiometry in SrTiO₃. *J Electrochem Soc*. 1981 Aug;128(8):1762–9.
45. Shin C-J, Yoo H-I, Lee C-E. Al-doped SrTiO₃: Part I, anomalous oxygen nonstoichiometry. *Solid State Ionics*. 2007;178(15):1081–7.
46. Waser R. Bulk conductivity and defect chemistry of acceptor-doped strontium titanate in the quenched state. *J Am Ceram Soc*. 1991;74(8):1934–40.
47. Han K, Lin Y-C, Yang C-M, Jong R, Mul G, Mei B. Promoting photocatalytic overall water splitting by controlled magnesium incorporation in SrTiO₃ photocatalysts. *ChemSusChem*. 2017;10(22):4510–6.
48. Noland JA. Optical absorption of single-crystal strontium titanate. *Phys Rev*. 1954 May;94(3):724.
49. Glickstein JJ, Salvador PA, Rohrer GS. Multidomain simulations of coated ferroelectrics exhibiting spatially selective photocatalytic activity with high internal quantum efficiencies. *J Mater Chem A*. 2016;4(41):16085–93.

SUPPORTING INFORMATION

Additional supporting information may be found in the online version of the article at the publisher's website.

How to cite this article: Zhang M, Salvador PA, Rohrer GS. Influence of particle size and shape on the rate of hydrogen produced by Al-doped SrTiO₃ photocatalysts. *J Am Ceram Soc*. 2022;105:5336–5346.
<https://doi.org/10.1111/jace.18488>